JURNAL SAINS MATERI INDONESIA (JUSAMI)
ISSN: 1411-1098 (print), 2614-087X (online)
VOL. 24, ISSUE 1, October 2022
DOI: https://doi.org/10. 10.17146/jsmi.2022.24.1.6667

ORIGINAL ARTICLE

Effect of Thermomechanical Treatment Combination on Electrochemical Behaviour of Nickel-Free Stainless-Steel Fe-10Mn-16Cr-3Mo

M. Rohmah*, F.M. Ridlo, D Irawan, R Roberto and P. A. Paristiawan

Research Center for Metallurgy, National Research and Innovation Agency (BRIN), Indonesia

ABSTRACT – Nickel-free stainless steel (NFSS) has emerged as a medical implant due to its excellent mechanical and corrosion properties. The toxic effect of nickel ion released in the conventional SS316L need to be addressed. As one of austenitizing elements used as nickel substitution, nitrogen is an important alloying element to improve the strength and resistance to pitting susceptibility. In this research, the nickel-free Fe-10Mn-16Cr-3Mo stainless steel has been developed. The effect of thermomechanical treatment consists of hot forging, hot rolling, cold rolling, and their combination followed by solution treatment on the electrochemical properties was further investigated. The corrosion resistance of Fe-10Mn-16Cr-3Mo was evaluated by the EIS and polarization test in Hank's solution at 37℃. A ferrite-austenite duplex structure was identified by microstructural investigation, with indistinct intermetallic phase at homogenized sample. Meanwhile, fully recrystallized grains and twinning structures were formed at thermomechanical samples, indicating in dynamic recovery and dynamic recrystallization. Furthermore, the potentiodynamic parameters demonstrates the protective oxide in all samples. However, sample #5 shows a lower current density, around 0.184 μA/cm^2, compared to other samples, indicating more protective passive film. In addition, the corrosion potential of sample #5, around 198 mV leading to higher corrosion resistance up to 0.02894 mmpy.

ARTICLE HISTORY
Received: 25 August 2022
Revised: 29 Sept 2022
Accepted: 12 Oct 2022

KEYWORDS
Nickel-free stainless steel
Fe-10Mn-16Cr-3Mo
Thermomechanical combination
Corrosion

INTRODUCTION

Several metallic materials are used as medical implants, such as stainless SS316L (contains 2–3 wt.% Mo, 13–15 wt.% Ni, and 17–19 wt.% Cr), Co-Cr alloy (9–35 wt.% Ni), and NiTi alloy, which may release nickel (Ni), iron, and chromium ions when corroded in body fluid environment. In the case of prolonged contact, the accumulated released nickel could induce an inflammatory type IV hypersensitivity reaction, allergic dermatitis reaction, and even cancer due to the formation of new tissue around metals. Because of this problem, some countries of the European Union Nickel Directive (94/27/EC) and the US restricted the nickel in specific products for direct and prolonged skin contact in the human body. The most important factor in determining nickel hypersensitivity risk for the medical implant is nickel release rather than nickel content in its alloy [1]. Ni concentrations in tissues near 316L plates and screws ranged from 116 to 1200 mg/L. In patients with Ni-containing alloy implants, the maximum rate of released Ni due to corrosion is estimated to be 20 mg/kg/day [2], [3]. Unfortunately, SS316L high prone to localized corrosion and fretting debris like pitting, crevice, and stress corrosion cracking in the body environment [4], [5]. To minimize the allergic risk, the nickel-free stainless steel, generally, the Fe-Cr-Mn-Mo-N system, was intriguingly proposed as an alternative to replacing the austenitic stainless steel for medical implant application due to its high mechanical properties, better corrosion resistance, low-cost production, and lower nickel content [6], [7]. On the other hand, nickel acts as an austenitic stabilizer which has the most substantial positive effect in providing non-ferromagnetic, excellent strength and toughness, good elasticity, fatigue endurance, and wear resistance on mechanical properties of stainless steel [2]. In addition, to maintain mechanical properties, the potentially detrimental effect of nickel ions released could avoid in human health through a new alloy design involving substituting Ni with N or Mn or both. Nitrogen (N), as interstitial alloying, is typically believed to improve the austenite stability, enhance strength hardness, work hardening rate, and fatigue resistance, as well as to avoid the ferritic phase formation [5]. On the other side, nitrogen alloying can improve passivation ability and reduce pitting susceptibility.

The superior mechanical and corrosion performances depend strongly on grain refinement and volume partitioning between austenite and ferrite phases in nickel-free stainless steel. Wang et al. [8] concluded that yield strength could be improved without strain-induced martensite formation by precipitation strengthening and work-hardening mechanisms, such as hot and cold rolling. Unfortunately, the hot and cold working seriously decreased the pitting corrosion resistance due to the dislocation density, martensite formation, residual stress, and secondary phase formation [9], [10]. The chemical composition must be balanced to prevent secondary phase formation, such as chromium-rich carbides, nitrides, and residual δ-ferrite. The secondary phase formation depends on the austenite stability and the rolling condition (the

*CORRESPONDING AUTHOR | M. Rohmah | ✉ miftakhur.rohmah@brin.go.id

strain rate, degree reduction, and rolling temperature). When the deformation temperature is low, or the strain rate and total amount of deformation are high, the intermetallic phase will be increased [9]. Therefore, an alternative processing method for preventing secondary phase formation of rolled NFSS without sacrificing strength and corrosion resistance is highly required.

The grain size and phase composition in uniform microstructure must be strictly controlled in the thermomechanical process by forging [11], hot rolling [12], and cold rolling [13]. However, only a few have investigated the combination processes. The secondary phase was not achieved by solution treatment. Nickel-free high nitrogen steel has produced a smaller grain size of ~43 µm without martensite formation after thermomechanical application in terms of 20% cold working followed by water quenched [9]. With an increased degree of cold or hot working, the ultimate tensile, yield strength, and the pitting potential increased [14]. However, the higher duplex alloy does not suffer decreased corrosion resistance after deformation [15]. After a preliminary cold or hot deformation, the high plasticity of X18H10 steel with 0.22% N was achieved by varying degree reduction up to 80% and attributed to the transformation induces plasticity (TRIP) effect, resulting in pronounced softening processes (dynamic recrystallization) [16]. Inappropriate forging and rolling parameters could embrittle the nickel-free stainless due to the precipitation initiation and growth. Therefore, this work aims to investigate further the effect of the thermomechanical process on the microstructure and corrosion resistance of Fe-10Mn-16Cr-3Mo steel. The forging and rolling conditions are carefully selected. Nickel-free stainless steel is typically produced using complex technologies, such as an induction furnace, plasma arc melting furnace, pressurized electro-slag remelting (ESR) method, argon oxygen decarburization (AOD), and powder metallurgy route [6]. Compared to other methods, producing a nickel-free stainless via an induction furnace is technically possible due to the faster melting, more energy efficiency, and economically attractive, by adding the high nitrogen additive (Ferro-nitride or CrN).

EXPERIMENTAL METHOD

Materials and Instruments

The sample used in the current study is a nickel-free stainless-steel, Fe-10Mn-16Cr-3Mo, with the chemical composition given in Table 1. The steel was produced by a melting process using an inductotherm furnace. The raw materials, such as steel scrap, ferromanganese, and ferrochrome, were all melted at 1700–1800°C. Afterward, the Ferro-nitride was added for nitrogen adjustment in optimal solubility of Fe-10Mn-16Cr-3Mo steel as a nickel replacement. The Y-block ingot was cast once the molten metal had reached composition homogeneity. Based on the calculation of Ni and Cr equivalent (Equation 1–2), Fe-10Mn-16Cr-3Mo has 21.29 points for Cr equivalent and 5.31 points for Ni equivalent [15], so when plotted on the Modified Schiffer diagram, it will be in the austenite-martensite-ferrite of phase tendency.

Table 1. Chemical composition of Fe-10Mn-16Cr-3Mo nickel free-stainless steel

Element	C	Mn	Cr	Ni	Mo	N	Cu	Si	Fe
Wt.%	0.05	9.95	16.64	0.15	2.98	0.2	0.31	0.38	Bal

$$Cr_{equivalent} = Cr + 0.7Si + 1.25Mo + 0.05\ Mn \quad (1)$$

$$Ni_{equivalent} = Ni + 27.4C + 22.7N + 0.35\ Cu \quad (2)$$

Method and Procedure

The steels were subjected to homogenizing at 1100°C for 3 hours, followed by air-cooling to ensure the removal of the casted structure. The result of this process was called as-homogenized (sample #1). In this study, the schematic of thermomechanical addition in Fe-10Mn-16Cr-3Mo stainless steel was illustrated in Figure 1 and the sample code was listed in Table 2. The thermomechanical, including hot and cold deformation, was added after homogenizing. The five pieces of a homogenized slab with a thickness of 10 mm were prepared for hot forging sample. The steel was austenitized at 1050°C for 1 hour and subsequent hot forging with 50-kN of a single punch to obtain the half reduction of slab thickness (~4.8mm), according to Figure 1(a). Next, the multiphase-hot rolling (Figure 1(b)) was conducted at 1050°C for 30% and 50% reduction to obtain the final thickness of ~3.46 mm and ~2.58 mm, respectively. Cold rolling (Figure 1(c)) was processed to 1.5 mm thick (~50% reduction in thickness). After hot forging/hot rolling/cold rolling, each sample was subsequently treated at 1050°C for 0.5 hours, followed by water quenched to prevent the secondary phase.

Table 2. Sample description in this work

Sample Code	Description
Sample #1	As homogenized + solution treatment
Sample #2	Hot forging 50% + solution treatment
Sample #3	Hot forging 50% + hot rolling 30% + solution treatment
Sample #4	Hot forging 50% + hot rolling 50% + solution treatment
Sample #5	Hot forging 50% + hot rolling 40% + cold colling 50% + solution treatment

Based on ASTM E3 standard, prior to the microstructural observation, all samples were ground with SiC abrasive paper and then polished with alumina slurry 1–0.5 µm. After obtaining the mirror-like surface, the sample was swab etched for a few seconds in Aqua regia, a mixture of 60 mL hydrochloric acid and 20 mL nitric acid. Correctly etched samples were observed on an Olympus BX-53M optical microscope (in accordance with ASTM E4). The average of grain size was calculated by the Intercept method (ASTM E112). The Jmatpro software was used to predict the microstructure formation by inputting specific chemical compositions (Table 1) and other solidification parameters (heating and cooling rate).

The electrochemical properties were carried out on Autolab 302 Multi BA electrochemical working station with Hank Solution (pH 7.4) as an electrolyte solution. Hank's solution was made from 8.0 g/L sodium chloride (NaCl), 0.40 g/L potassium chloride (KCl), 0.35 g/L sodium bicarbonate ($NaHCO_3$), 0.25 g/L (sodium dihydrogen phosphate dihydrate) $NaH_2PO_4.2H_2O$, 0.06 g/L dipotassium phosphate (KH_2HPO_4), 0.19 g/L calcium chloride ($CaCl_2$), 0.19 g/L magnesium chloride ($MgCl_2$), 0.06 g/L magnesium sulphate heptahydrate ($MgSO_4.7H_2O$), and 1 g/L D-glucose in 1000 mL distilled water. The potentiodynamic and the electrochemical impedance spectroscopy (EIS) were performed in the three-electrode glass cell system with Fe-10Mn-16Cr-3Mo acting as a working electrode, the Platina wire employed as the counter electrode, and Ag/AgCl as a reference electrode. The electrochemical tests were carried out at 37°C temperatures after subjecting the sample to open circuit potential for 30 minutes. The EIS was performed in the frequency ranges from 10^{-1} to 10^5 Hz and with an amplitude of 10 mV, referred to as open circuit potential (Vocp). The potentiodynamic was conducted 1 mV/s scan rate in swept potential from -0.5 to +1 V. The result of EIS and potentiodynamic was fitted using Nova 1.11.

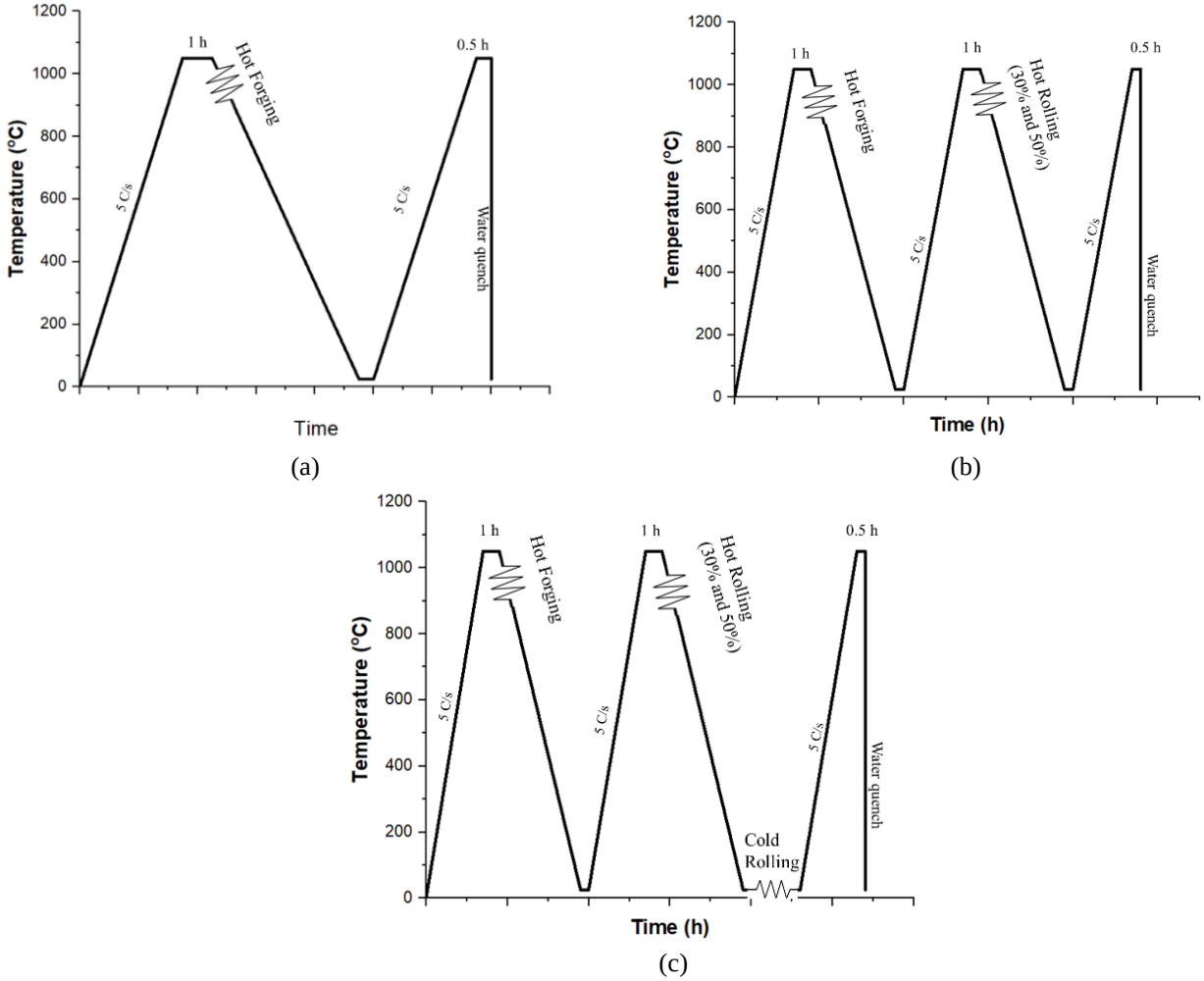

Figure 1. Schematic diagram of (a) hot forging sample, (b) hot forging + hot rolling sample, and (c) hot forging + hot rolling + cold rolling sample

RESULTS AND DISCUSSION

Microstructure Analysis

Phase solidification of Fe-10Mn-16Cr-3Mo was calculated using JMatPro version 12.2 for formed phase prediction. The model simulation assumes that solute has a slower diffuse in the solid phase. The result of the simulation depicted in Figure 2.

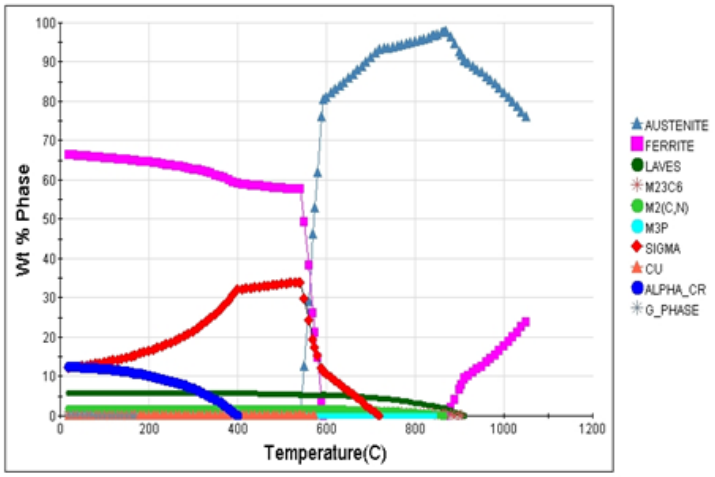

Figure 2. Phase solidification of Fe-10Mn-16Cr-3Mo nickel-free stainless steel using JMatpro simulation

Generally, the Fe-10Mn-16Cr-3Mo consists of 76.35 % austenite (γ) and 23.65% ferrite (α); thus, its steel was classified as nickel-free-duplex stainless steel. The volume fraction between austenite and ferrite was disproportioned due to low nickel and high manganese content [16]. At temperatures under 700 °C, the composition of Fe-10Mn-16Cr-3Mo can lead to the formation of intermetallic phase: sigma (σ) phase, laves phase, carbide ($M_{23}C_6$, M_3P), and nitrides. These precipitate phases will decrease the corrosion resistance of the steel. As mentioned before, the hot deformation behaviour of Fe-10Mn-16Cr-3Mo is complex due to the coexistence of multiphase (ferrite, austenite, and a few martensites). In other that, the microstructure evolution has closed attention for this study. The effect of the hot deformed process on the microstructure was observed in Figure 3.

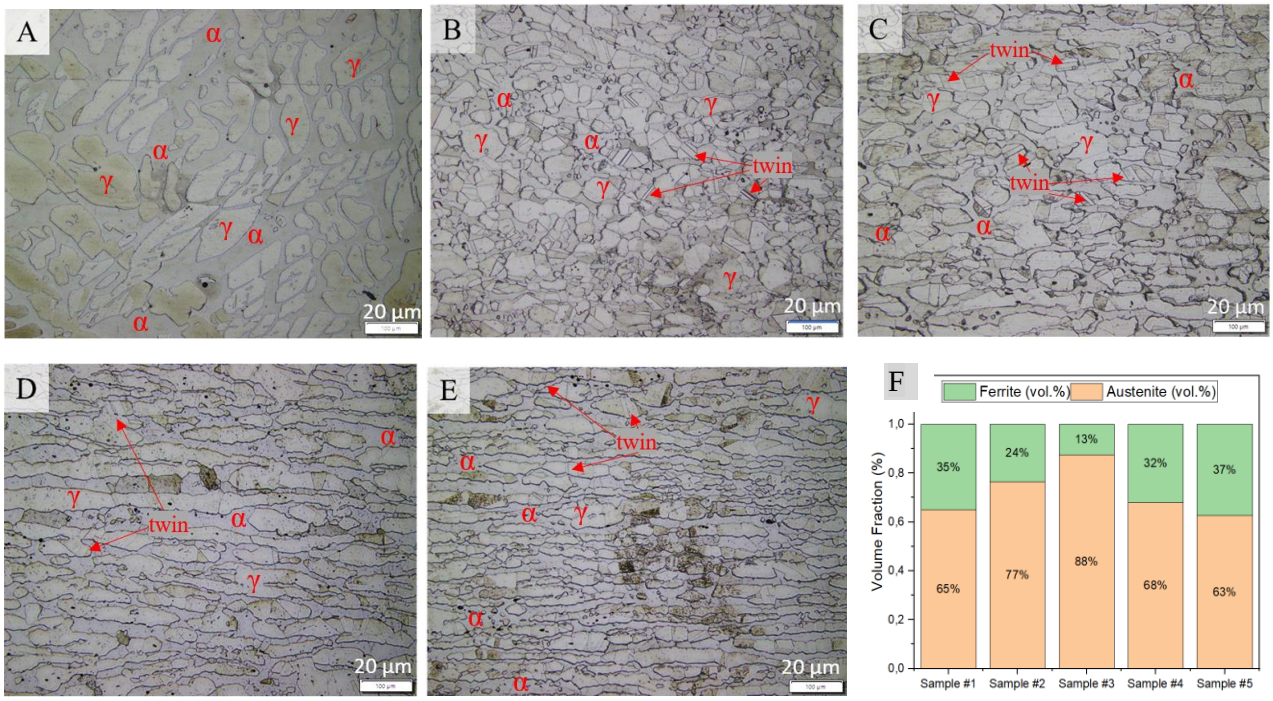

Figure 3. Microstructure of Fe-10Mn-16Cr-3Mo nickel-free-stainless steel after (a) as homogenized, (b) hot forging, (c) hot forging + hot rolling 30%, (d) hot forging + hot rolling 50%, (e) hot forging + hot rolling + cold rolling 50%, and (f) austenite-ferrite of volume fraction in all samples – (α = ferrite, γ = austenite, twin = twin structure)

The microstructure of the homogenized sample is a type of two-phase microstructure that comprises the irregular island of ferrite (α) structure with coarse grains in the austenite (γ) matrix (Figure 3(a)). Chromium promotes a ferritic structure, and nitrogen addition promotes an austenitic structure. The distribution of austenite islands is uniform without specific orientation. Their austenite-ferrite mixed microstructures were similar to Halimi et al. results [17], which provided a combination of the corrosion resistance and increased strength. European Patent Number EP2575674A2 claimed that the duplex structure was applied for the endoprosthesis (stent) [18]. The intermetallic phase was not clearly visible in all microstructures because the solution treatment could dissolve it in the matrix. The grain size of the sample

after hot forging is smaller and more equiaxed than in homogenized conditions (Figure 3(a)–(b)), indicating that the dynamic recrystallization occurs through the forging process leading to new grains formation.

After hot rolling, the microstructure changes significantly in the ferrite regions, with fully recrystallized grains and numerous twins in the α matrix (Figure 3(c)–(e)). A twin structure has a significant reorientation of the lattice due to a shearing process caused by mechanical deformation. In the 30% reduction of hot-rolled, the austenite grain was partially elongated and decreased proportionally, resulting from work hardening and transformation into twins (Figure 3(c)) [19]. As the reduction increased, the mechanical twins without undissolved precipitate were clearly observed inside the grain one, related to the inhibiting dislocation movement. The deformation is determined by the stacking fault energy (SFE) and elastic-plastic properties. Austenite has low SFE and plastic deformation, creating the partial dislocation and overlap stacking fault and giving rise to a twin [20]. According to the JmatPro simulation, the value of stacking fault energy is 204.9 mJ/m^2, which suppresses a twin formation.

Since hot deformation, the ferrite leads to the dynamic recovery mechanism and the austenite preferentially in dynamic recrystallization [21]. Moreover, the austenite became a discontinuous island-shaped structure (Fig 3(e)) due to the Mn content having maintained a mechanical twinning during cold-rolling [22]. It can be seen that the cold rolling reduces the phase fraction and grain size of ferrite. The average grain diameter for sample #1, sample #2, sample #3, sample #4, and sample #5 in succession is 34.2 µm, 31.8 µm, 24.432 µm, 10.08 µm, and 10.336 µm. In addition, the austenite fraction result is 65%, 76.5%, 87.5%, 68%, 62.75% for sample #1, sample #2, sample #3, sample #4 and sample #5, respectively (Figure 3(f)).

Polarization and EIS Analysis

The corrosion test predicted the interaction between Fe-10Mn-16Cr-3Mo steel and electrolyte Hank solution, adopted in the human body for medical implant purposes. In this study, the focus on medical materials is inert, do not chemically react, and are resistant to localized corrosion. The potentiodynamic curves of Fe-10Mn-16Cr-3Mo are shown in Figure 4. For detailed information, the potentiodynamic parameter, including corrosion potential, current density potential, passivity, and breakdown or pitting potential, obtained by Tafel fitting, were listed in Table 3.

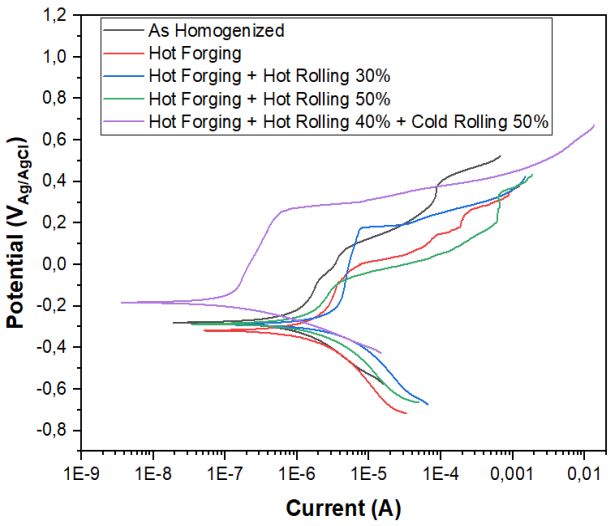

Figure 4. Potentiodynamic of Fe-10Mn-16Cr-3Mo nickel-free-stainless steel in Hank solution

Figure 4 demonstrates the thermomechanical addition effect on the anodic dissolution behavior of Fe-10Mn-16Cr-3Mo in Hank's solution. Basically, the all-curve shapes are nearly identical, each curve exhibits a passive and trans-passive region, indicating the protective oxide and breakdown (Epit) film is formed on the metal surfaces due to the oxygen evolution. The pit preferentially occurred in the ferritic phase [14]. The corrosion potential (*Ecorr*) and passivity potential (*Epass*) shifted to more negative direction along with the hot forging and hot rolling addition, referring to the corrosion resistance decreasing after hot deformation. A deformed sample has residual stress and dislocation density which is not beneficial in corrosion resistance [23]. In this work, for all conditions, the anodic slope (βa) is much steeper than the cathodic slope (βc), indicating that the spontaneous passivation occurred in the anodic branch. The critical potential of active to passive transition (*Epass*) also showed a very similar trend of potential shift, approximately -231 to -103 mV for passivation and near to +7.02 to +271.8 mV for trans-passivation zone. In this region, the passive film remained stable. Sample #5, with all thermomechanical types, generated more expansive passivation zone which was attributed to the interaction between metals and species aggressive ion of Hank's solution that might form a passive film with high passivation ability. In the presence of chloride ions and the potential increases, the passive layer becomes unstable and produces a localized corrosion with pit formation [9].

According to Table 3, the corrosion potential of sample #5 is more positive, around -198.03 mV, indicating this treatment produces nobler and higher corrosion resistance. The uniform island structure provides a moderate corrosion

rate, of 0.02894 mmpy for sample#1 and 0.0204 mmpy for sample#2. With the lower current density, around 0.184 µA/cm^2, the passive film formed on sample #5 is more protective. In addition, the galvanic activities between ferrite and austenite might accelerate the growth of the passive film [24].

Table 3. Potentiodynamic parameters of Fe-10Mn-16Cr-3Mo using Tafel extrapolation fit

Sample	Ba (mV/dec)	Bc (mV/dec)	Ecorr (mV)	Icorr (µA/cm^2)	CR (mmpy)	Epass (mV)	Epitt (mV)	Ref
Sample #1	283.2	501.2	-280.84	2.494	0.02894	-157.7	--	*
Sample #2	259.8	358	-317.93	1.758	0.02040	-231	7.02	*
Sample #3	354.2	9910	-288.95	3.962	0.04597	-198.3	180.5	*
Sample #4	233.1	1475.7	-285.64	3.120	0.03621	-228.6	60.7	*
Sample #5	115.28	1001.8	-198.03	0.184	0.00213	-103.6	271.8	*
SS316L	3202	5546	-655	5.556	2359	-300	403	[6]
Fe-18Cr-12Mn-N	78.5	61	-495.4	2.090	unreport	-350	-70	[22]
Ti-6Al-4V	-	-	-405	0.031	-	0	1200	[23]

*this work

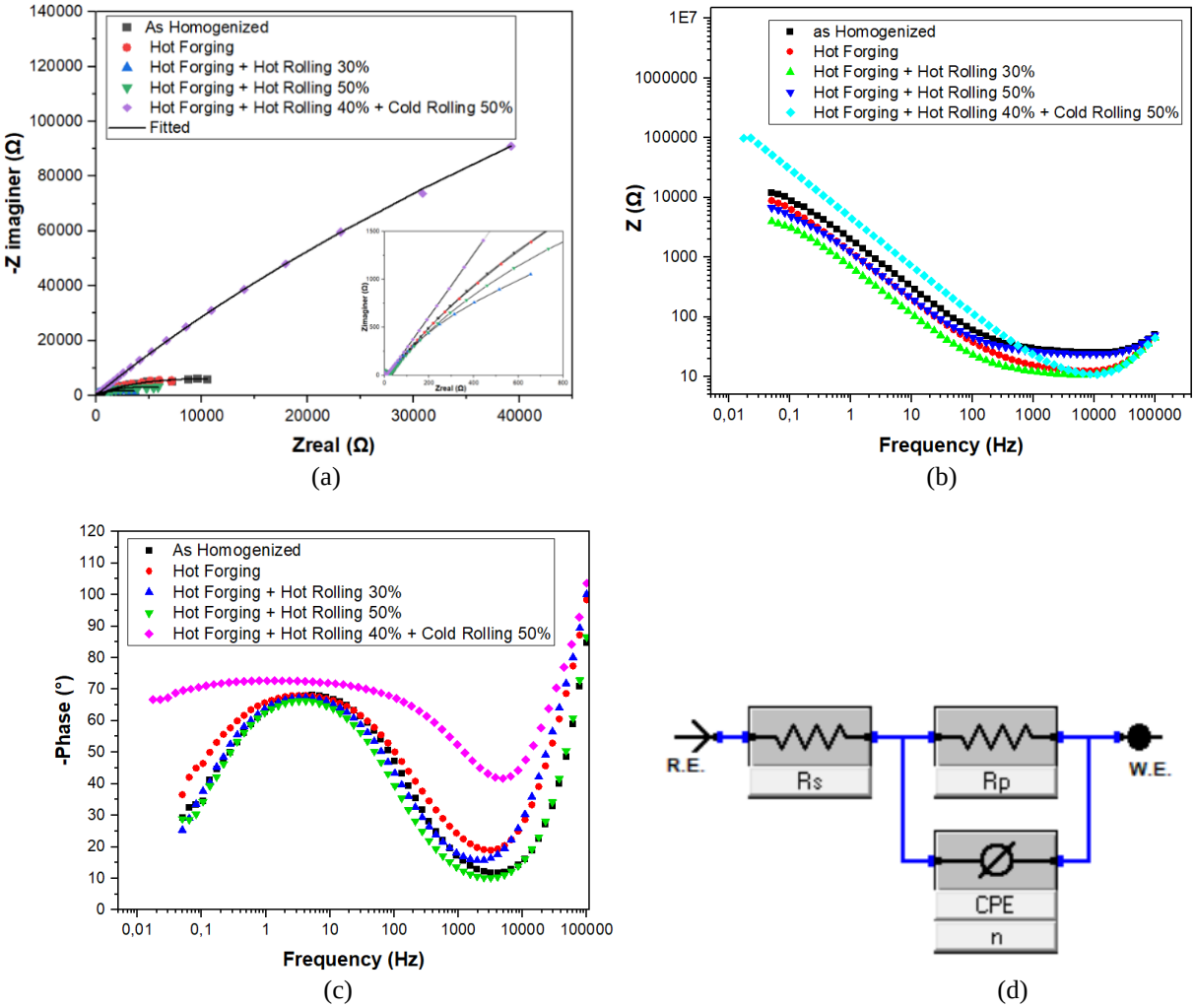

Figure 5. EIS spectra for (a) Nyquist, (b) Bode Modulus, (c) Bode Phase, and (d) Equivalent Electric Circuits fit of Fe-10Mn-16Cr-3Mo nickel-free stainless steel in Hank solution

To investigate the corrosion behavior at Fe-10Mn-16Cr-3Mo alloy/solution interface, Nyquist and Bode plots were recorded and depicted in Figure 5. Impedance spectra were analyzed in terms of the equivalent electric circuits (EECs) presented in Figure 5(d) to obtain the EIS parameters value, including the solution resistance (Rs), polarization resistance (Rp), constant phase element (CPE) or charge transfer resistance, and parameter of CPE (n). The exponent "n" of CPE determines the capacitive or inductive behavior of the impedance arc. At $0.5 < n < 1$, the CPE is a non-ideal capacitor directly related to the electrode roughness and heterogeneities [25]. All Nyquist plots have only one unfinished semicircle of capacitor arc (Figure 5(a)), the impedance of bode modulus is quite high in the low frequency (Figure 5(b)), and the phase angles are close to 90° in the 1–100 Hz frequency (Figure 5(c)). The radius, diameter of capacitor arc, and maximum phase angle decrease which mean the passive film formed is destroyed and inversely to corrosion rate by

thermomechanical addition. The larger diameter (|Z'| vs. |Z"| value) of impedance arc obtained by cold rolled addition, which indicated the higher charge transport or solution resistance, is due to the harder corrosion occurred and higher stability of the passive film on the surface. The homogenized and hot-forged samples have similar radius angles and different arc circle lengths, indicating the corrosion parameter is closely identical. However, the passivity stabilization of hot-forged sample is longer due to grain refinement [26]. More grain refinement boundaries may improve chromium diffusion and promote compact passive film formation. Ferrite is expected to be nobler than austenite due to the lower electrochemical activity and the enrichment of Fe, Cr, Mo, and W [24]. These results are in close agreement with those obtained from the potentiodynamic test.

Table 4. EIS parameter of Fe-10Mn-16Cr-3Mo nickel-free stainless steel

Sample	Rs (Ω)	Rp (MΩ)	CPE mMho	n
Sample #1	22.568	19.5	0.1311	0.995
Sample #2	11.043	16.94	0.197	0.771
Sample #3	2.8164	5.187	0.3247	0.996
Sample #4	22.836	8.488	0.1889	0.786
Sample #5	61.961	9.82 E7	522.1	0.780

The EIS parameters in Table 4 reveal that the thermomechanical addition increases a charge transport resistance in Hank solution. The highest Rs and Rp values are about 61.961 Ω and 9.82×10^7 MΩ. It is suggested that the cold rolling addition at the end of the thermomechanical process effectively improve the capacitive behaviour and corrosion resistance due to the changes of volume fraction between austenite and ferrite (62.75 vol.% austenite-37.25% vol.% ferrite). The lowest austenite fraction (α/γ ratio close to 0.593), the smaller grain size (10.336 μm), and the presence of mechanical twin structure synergistically improved the corrosion resistance by providing wide passivation. Our previous research stated that the high passivation is caused by the higher chromium content in the nickel-free stainless steel [27].

CONCLUSION

The harmful effects of nickel ion released in the human body cause a development of Fe-10Mn-16-3Mo nickel-free stainless steel as medical implant. The microstructure of Fe-Cr-Mn-Mo-N series nickel-free stainless steel is a duplex structure that consists of coarse grain ferrite in the austenitic matrix. A higher volume fraction of austenite was promoted by nitrogen and high manganese addition, whereas ferrite promotes by chromium. Furthermore, dynamic recovery and recrystallization have contributed to fully recrystallized grains and twinning structures after thermo-mechanical treatment. The combination of all thermomechanical treatments obtained the grain refinement up to ~10.08 μm and ~10.336 μm for samples #4 and #5, respectively. According to potentiodynamic and EIS observations in Hank's solution, the addition of cold rolling at the end process significantly increased the capacitive behavior (i.e., 61.961 of Rs and 9.82 × 107 M of Rp) and corrosion resistance due to changes in the volume fraction between austenite and ferrite (i.e., 62.75 vol.% austenite-37.25% vol.% ferrite). The corrosion rate of all samples is lower than stainless 316L, suggesting that this alloy can replace its role in implant alloys. With cold rolling addition, the large passivation was obtained, ranging from -103.6 mV to -271.8 mV. The wide passivation was closely correlated with the synergistic effect between the lowest austenite fraction (α/γ ratio close to 0.593), the smaller grain size (10.336 μm), and the presence of a mechanical twin structure. Compared to all thermo-mechanical treatment types, the combination of hot forging, hot rolling, and cold rolling has yielded lower current density, indicating a more protective passive film leading to the higher corrosion resistance of the sample in Hank's electrolyte solution. In addition, more grain refinement boundaries are believed to promote compact passive film formation.

ACKNOWLEDGEMENT

All authors could like thanks to Research Center for Metallurgy – BRIN for the fund and research facilities.

REFERENCES

[1] K. A. Pacheco. "Allergy to Surgical Implants." *Clin. Rev. Allergy Immunol.*, vol. 56, no. 1, pp. 72–85, Sep. 2019.
[2] K. Yang, Y. Ren, and P. Wan. "High nitrogen nickel-free austenitic stainless steel: A promising coronary stent material." *Sci. China Technol. Sci.*, vol. 55, no. 2, pp. 329–340, Feb. 2012.
[3] K. Yang and Y. Ren. "Nickel-free austenitic stainless steels for medical applications." *Sci. Technol. Adv. Mater.*, vol. 11, no. 1, p. 014105, Feb. 2010.
[4] C. A. Baumann and B. D. Crist. "Nickel allergy to orthopaedic implants: A review and case series." *J. Clin. Orthop. Trauma*, vol. 11, pp. S596–S603, Feb. 2020.
[5] M. Li *et al.* "Study of biocompatibility of medical grade high nitrogen nickel-free austenitic stainless steel in vitro." *Mater. Sci. Eng. C*, vol. 43, pp. 641–648, Oct. 2014.

[6] M. Talha, C. K. Behera, and O. P. Sinha. "A review on nickel-free nitrogen containing austenitic stainless steels for biomedical applications." *Mater. Sci. Eng. C*, vol. 33, no. 7, pp. 3563–3575, Jun. 2013.
[7] L. Patnaik, S. R. Maity, and S. Kumar. "Status of nickel free stainless steel in biomedical field: A review of last 10 years and what else can be done," *Mater. Today Proc.*, vol. 26, no. 2, pp. 638–643, 2019.
[8] Y. Wang, Y. Wang, and Z. Wang. "Enhancing yield strength of high nitrogen austenitic stainless steel." *J. Constr. Steel Res.*, vol. 187, no. May, p. 106927, Dec. 2021.
[9] M. Talha, C. K. Behera, and O. P. Sinha, "Effect of nitrogen and cold working on structural and mechanical behavior of Ni-free nitrogen containing austenitic stainless steels for biomedical applications," *Mater. Sci. Eng. C*, vol. 47, pp. 196–203, Feb. 2015.
[10] J. Li *et al.* "Enhancing Pitting Corrosion Resistance of Severely Cold-Worked High Nitrogen Austenitic Stainless Steel by Nitric Acid Passivation." *J. Electrochem. Soc.*, vol. 166, no. 13, pp. C365–C374, 2019.
[11] B. B. Singh *et al.* "A Comparative Study on the Ballistic Performance and Failure Mechanisms of High-Nitrogen Steel and RHA Steel Against Tungsten Heavy Alloy Penetrators." *J. Dyn. Behav. Mater.*, vol. 7, no. 1, pp. 60–80, 2021.
[12] J. Lal, S. Kumar, and N. C. S. Srinivas. "Effect of Preliminary Cold Working on High-Temperature Tensile Behavior of Nickel-Free High-Nitrogen Austenitic Steel." *Met. Sci. Heat Treat.*, vol. 61, no. 7–8, pp. 478–481, 2019.
[13] L. M. Kaputkina, M. G. Medvedev, V. G. Prokoshkina, I. V. Smarygina, and A. G. Svyazhin. "Influence of alloying by nitrogen on the strength and austenite stability of X18H10 steel." *Steel Transl.*, vol. 44, no. 7, pp. 502–508, 2014.
[14] N. Fuertes and R. Pettersson. "Effect of cold rolling on microstructure, corrosion and electrochemical response of the lean duplex stainless steel LDX 2101® by a correlative EBSD–SKPFM investigation." *Mater. Corros.*, vol. 71, no. 7, p. 1052–1065, 2020.
[15] F. Ruffini *et al.* "Modelling approach to support design of new high nitrogen austenitic steel for wind turbines components." *Wind Eng.*, vol. 40, no. 5, pp. 419–425, Aug. 2016.
[16] R. M. Santos, D. G. Rodrigues, M. L. Dias Santos, and D. B. Santos. "Martensite reversion and strain hardening of a 2304 lean duplex stainless steel subjected to cold rolling and isochronous annealing at low temperatures." *J. Mater. Res. Technol.*, vol. 16, pp. 168–186, 2022.
[17] A. D. Halimi, Sulistijono, and M. I. P. Hidayat. "Microstructural characterization of super duplex stainless steel UNS S32760 after heat treatment in different cooling media," in *AIP Conference Proceedings*, 2020, vol. 2296, no. April 2021, p. 020077.
[18] I. G. S. Sandhu, R. D. Simari, D. R. Holmes, M. D. D. Daescu, and A. P. Parakka. "Medical devices including duplex stainless steel." U.S. Patent Application No. US 2013/0211537 A1, Aug. 15, 2013.
[19] G. G. B. Maria, C. A. D. Pedroso, D. G. Rodrigues, and D. B. Santos. "Strain-Induced Martensite and Reverse Transformation in 2304 Lean Duplex Stainless Steel and its Influence on Mechanical Behavior." *Steel Res. Int.*, vol. 90, no. 3, pp. 1–11, 2019.
[20] V. S. A. Challa, X. L. Wan, M. C. Somani, L. P. Karjalainen, and R. D. K. Misra. "Strain hardening behavior of phase reversion-induced nanograined/ultrafine-grained (NG/UFG) austenitic stainless steel and relationship with grain size and deformation mechanism." *Mater. Sci. Eng. A*, vol. 613, pp. 60–70, 2014.
[21] R. Badji, B. Cheniti, C. Kahloun, T. Chauveau, M. Hadji, and B. Bacroix. "Microstructure, mechanical behavior, and crystallographic texture in a hot forged dual-phase stainless steel." *Int. J. Adv. Manuf. Technol.*, vol. 116, no. 3–4, pp. 1115–1132, 2021.
[22] D. M. Bastidas, J. Ress, J. Bosch, and U. Martin. "Corrosion mechanisms of high-mn twinning-induced plasticity (Twip) steels: A critical review." *Metals*, vol. 11, no. 2. pp. 1–45, 2021.
[23] V. Kumar, R. K. Gupta, and G. Das. "Influence of Forging and Annealing on the Microstructure and Corrosion Behavior of Austenitic Stainless Steel." *J. Inst. Eng. Ser. D*, vol. 101, no. 1, pp. 105–109, 2020.
[24] E. Rahimi, A. Kosari, S. Hosseinpour, A. Davoodi, H. Zandbergen, and J. M. C. Mol. "Characterization of the passive layer on ferrite and austenite phases of super duplex stainless steel." *Appl. Surf. Sci.*, vol. 496, no. May, p. 143634, 2019.
[25] H. Zhang *et al.* "Different corrosion behaviors between α and β phases of Ti6Al4V in fluoride-containing solutions: Influence of alloying element Al." *Corros. Sci.*, vol. 169, no. November 2019, 2020.
[26] A. Yilmaz, X. Li, S. Pletincx, T. Hauffman, J. Sietsma, and Y. Gonzalez-Garcia. "Passive Film Properties of Martensitic Steels in Alkaline Environment: Influence of the Prior Austenite Grain Size." *Metals (Basel).*, vol. 12, no. 2, Feb. 2022.
[27] M. Rohmah, F. M. Ridlo, Y. N. Thaha, P. A. Paristiawan, and N. R. Hakim. "e." *Eng. Appl. Sci. Res.*, vol. 49, no. 5, pp. 681–687, 2022.